Pergamon

Acta mater. 48 (2000) 3917–3930

Acta MATERIALIA

www.elsevier.com/locate/actamat

SENSITIVITY OF α-ZY4 HIGH-TEMPERATURE DEFORMATION TEXTURES TO THE β-QUENCHED PRECIPITATE STRUCTURE AND TO RECRYSTALLIZATION: APPLICATION TO HOT EXTRUSION

R. E. LOGÉ[1]*, J. W. SIGNORELLI[2], Y. B. CHASTEL[1], M. Y. PERRIN[1] and R. A. LEBENSOHN[2]

[1]Ecole des Mines de Paris/CEMEF, BP207, F-06904 Sophia Antipolis Cedex, France and [2]Instituto de Fisica Rosario (IFIR–CONICET), 27 de Febrero 210 Bis, 2000 Rosario, Argentina

(Received 24 November 1999; received in revised form 7 April 2000; accepted 5 June 2000)

Abstract—Hot extrusion of Zircaloy-4 tubes usually starts from β-quenched microstructures and induces strong textures. Individual crystallographic orientations were investigated by transmission electron microscopy using the electron backscatter pattern (EBSP) technique as well as Kikuchi patterns. Basal poles were found close to the tangential direction of the tubes in regions exhibiting fine and homogeneously distributed precipitates (FHDPs). In contrast, regions with large and isolated precipitates (LIPs) had more variable orientations. Laboratory plane strain compression tests were performed and the induced textures were compared with numerical simulations using a polycrystalline viscoplastic self-consistent model. The β-quenched material was modeled as a mixture of LIP and FHDP regions, each having a different set of slip system hardnesses, with a volume fraction depending on the previous thermal history. The model was subsequently applied to predict the texture evolution during extrusion with metadynamic recrystallization taking place thereafter. The calculation suggests that recrystallization modifies the orientation of those grains where ⟨c + a⟩ crystallographic slip has been significantly activated during deformation.

Keywords: Microstructure; Texture; High temperature; Zircaloy-4; Recrystallization and recovery

1. INTRODUCTION

Zircaloy-2 and Zircaloy-4 products have found a large range of applications in the nuclear industry, owing to their low probability of neutron capture and their resistance to high-temperature corrosion. In the sequence of forming processes leading to planar or tubular products, particular attention is usually paid to the induced crystallographic textures, as they dictate the extent of mechanical anisotropy of the final product. Indeed, Zircaloys are made primarily of zirconium (see Table 1) whose hexagonal symmetry [hexagonal close-packed (hcp)] lattice exhibits both elastic and plastic anisotropy [1, 2]. The plastic anisotropy can be attributed to the c-axis direction in the unit cell being the "hardest" one. During plastic deformation, and thus when texture is evolving, this anisotropy leads to predominant activity of slip systems with the ⟨11$\bar{2}$0⟩ or ⟨a⟩ Burgers vector [3].

Intermediate stages of forming processes of Zircaloy products are usually carried out in the high α-region; i.e., close to the phase transition between the hcp α-phase and the body-centered cubic (bcc) β-phase, around 1083 K. Textures resulting from hot rolling [4–6] or extrusion [7–10] of zirconium-based alloys have been studied in detail. The temperature

Table 1. Chemical compositions of Zircaloy-2 and Zircaloy-4 (wt%). The balance zirconium content is about 98 wt%

	Sn	O	Fe	Cr	Ni
Zircaloy-4	1.5	0.11	0.21	0.12	< 0.005
Zircaloy-2	1.5	0.11	0.13	0.12	0.05

* To whom correspondence should be addressed.

1359-6454/00/$20.00
PII: S1359-6454(00)00179-8

range of interest (873–1073 K) is, however, characterized by strong variations in many properties like ductility, stiffness and strain-rate sensitivity [11], and by many microstructural events like the change of preferential deformation modes [2, 12], recovery and recrystallization [13]. This is why slight variations in the forming process conditions (temperature or friction) or in the initial microstructure may induce substantial texture modifications [10, 11]. The role of temperature is particularly unclear since it influences both the relative slip system hardnesses [2, 12, 14] and the proportion of recovery and/or recrystallization [11, 13].

Hot extrusion of Zircaloy tubes usually involves dynamic recovery, and *metadynamic* recrystallization* [8, 11, 13]. The extents of these phenomena vary along the radial direction of the tubes, due to both the thermo-mechanical conditions of the process and the initial microstructure. For example, metadynamic recrystallization proceeds after extrusion, upon air cooling of the tube, as long as the temperature is in a good temperature range. The cooling rates are typically a few degrees per second, but vary along the radial direction. On the other hand, the *initial* microstructural gradient (i.e., before extrusion) comes from the water-quenching, or "β-quenching", operation. This quenching operation is performed on cylinders being heat-treated in the β-phase. Only after this operation is done, is the cylinder drilled into a tube and ready for extrusion. The cooling rate from the β-phase varies along the radial direction and dictates the type of *Widmanstätten* microstructure thereby obtained [16, 17].

In this paper we focus on the effect of the β-quenched microstructure on the high-temperature deformation textures of Zircaloy-4 (Zy4) in the 873–1023 K temperature range. The extrusion deformation path along the inner boundary of a tube is approximated by that of laboratory plane strain compression (PSC) tests. In these tests, two types of initial microstructure, typical of low and high cooling rates from the β-phase, are chosen to study the microstructure effects on texture evolution. Metadynamic recrystallization is avoided in most cases by using a constant and sufficiently low deformation rate. Parallel to the PSC tests, the microstructures of hot extruded samples are examined, and related to measurements of individual crystallographic orientations. A viscoplastic self-consistent polycrystalline model [18] is then extended to include the observed relevant microstructural features in texture calculations. The model is calibrated with respect to the PSC tests, and then used to predict extrusion textures. The complication arising from the recrystallization effects is finally discussed, as well as the physical interpretation of the selected set of slip system hardnesses and the relevance of the model.

* Here, *metadynamic* recrystallization designates the particular mechanism by which the structure starts recrystallizing right after deformation (no incubation period), provided that the temperature remains high enough. This kind of recrystallization initiates, like static recrystallization, only after some amount of deformation. However, unlike pure static recrystallization, its extent is also strongly related to the deformation *rate* applied to the material [15]. The deformation rate is assumed to influence the number of recrystallization nuclei formed during deformation.

2. EXPERIMENTAL WORK

This study used a set of Zy4 cylinders that had been heat-treated in the β-phase at 1323 K and subsequently water-quenched. The experimental work involved laboratory mechanical testing, i.e., PSC tests, as well as industrial hot extrusion tests. The PSC samples were cut from a single cylinder, either close to the external surface or far from it, giving two categories: the rapidly quenched (RQ) samples and the slowly quenched (SQ) samples, respectively. Hot extrusion tests were performed on tubes obtained by drilling along the center line of the β-quenched cylinders, as explained earlier.

2.1. Initial microstructure and texture

The microstructure varies along the radial direction of the cylinder as a function of the cooling rate from the β-phase. Two extreme cases are given by the SQ and RQ microstructures described above. They are illustrated in Fig. 1, using both optical microscopy and transmission electron microscopy (TEM).

With an optical microscope, the dependence of the platelet thickness on the cooling rate is clear [16]. At the TEM scale, this dependence is not as obvious because a narrow platelet was selected to illustrate the SQ microstructure. This allows us to visualize the interior of a platelet, and to compare the spatial distribution of precipitates with the RQ one. The precipitates are formed during cooling from the β-phase because of the very low solubility of both iron and chromium in the α-phase. In the SQ microstructures most of the precipitate volume fraction is made of large and isolated precipitates (LIPs), because the slow cooling rate allowed for some coarsening of the precipitates. In contrast, the RQ microstructure displays high volume fractions of fine and homogeneously distributed precipitates (FHDPs) inside the platelets, while coarser precipitates still appear at their boundaries. Some coarse precipitates also appear rarely inside the platelets, but they should not be confused with the long hydrides that have grown perpendicular to the platelet boundaries. These hydrides form at low temperature, and dissolve well before reaching the high α-region.

Fig. 2 shows how the initial texture varies along the thickness of the cylinder, which in turn gives the initial SQ and RQ textures, together with an intermediate one at mid-thickness. The (0002) pole figures exhibit several peaks of high intensity, but distributed quite randomly. The peaks can be attributed to colonies of α-platelets which grew, upon quenching, from

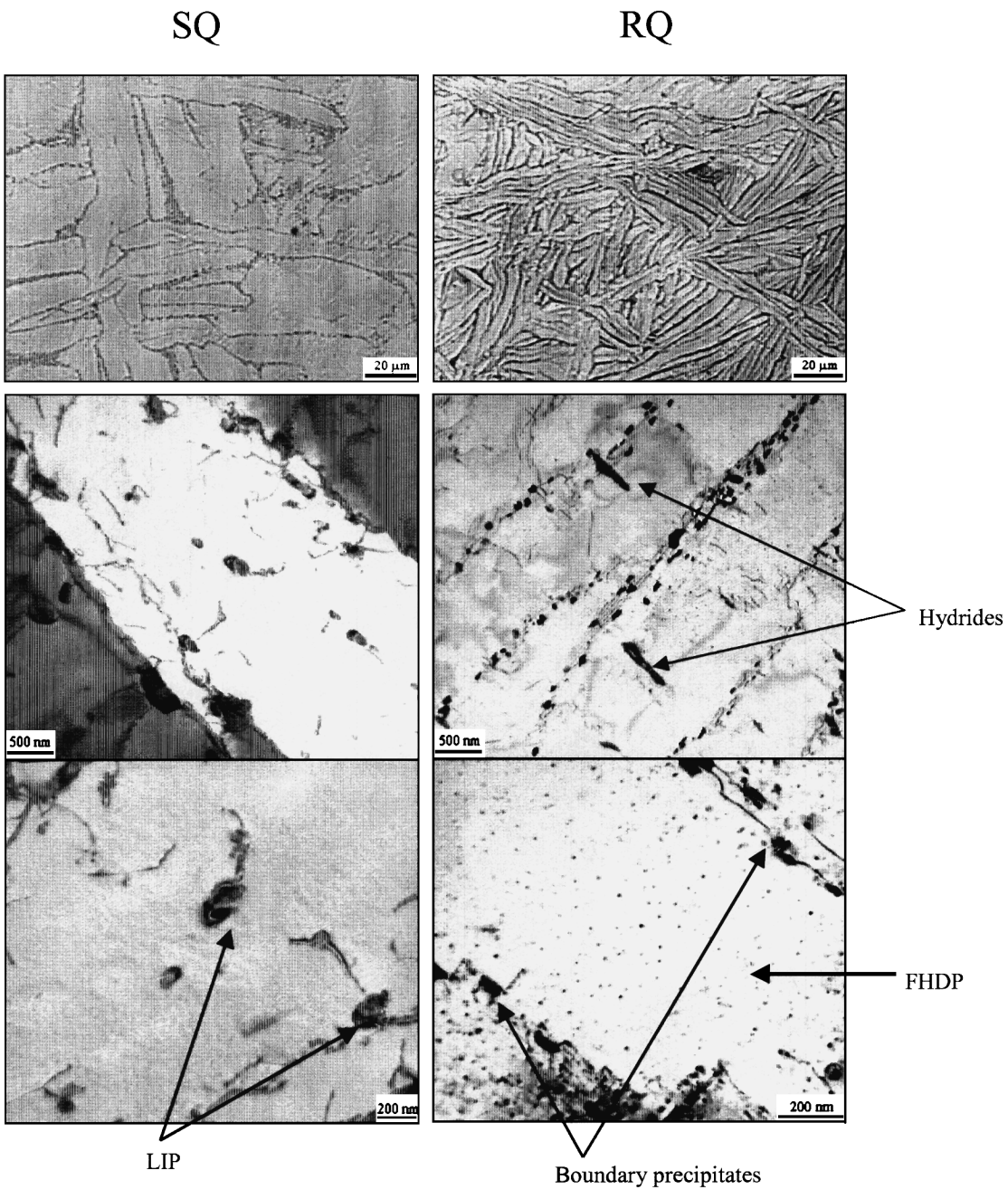

Fig. 1. Widmanstätten structures at different scales. RQ and SQ refer to rapidly and slowly quenched from the β-phase, respectively.

large β-grains, retaining close crystallographic orientations [19].

2.2. Plane strain compression (PSC) tests

As stated earlier, PSC tests were used to study the effect of a "rolling" deformation mode on texture evolution, without the complication of recrystallization phenomena if the combination of strain rate and temperature is well chosen. The plane strain deformation mode is used as a representation of the deformation path along the inner surface of a tube being extruded.

2.2.1. Experimental set-up. Fig. 3 shows the experimental configuration with the dimensions of the tools and the samples. These dimensions ensure a deformation mode close to ideal plane strain [20] in the deformed zone, all the way to the final thickness of 2.2 mm (62% reduction).

Tests were carried out at temperatures of 873, 923, 973 and 1023 K, and at strain rates of 0.1 s^{-1} and

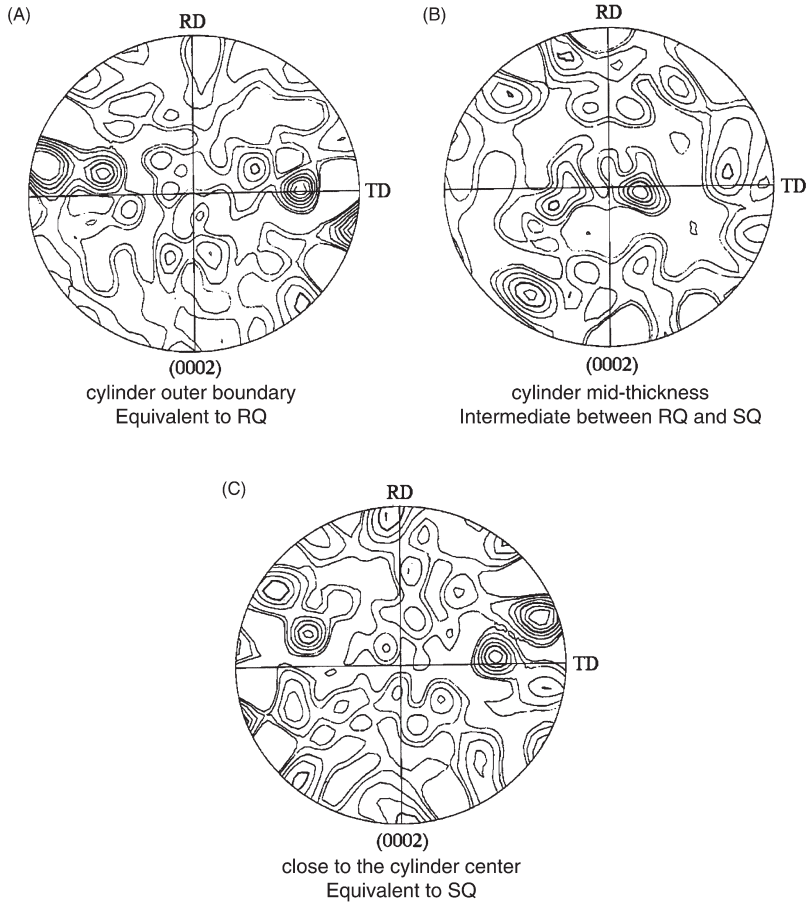

Fig. 2. Three initial (0002) pole figures at three different thickness levels in a β-quenched cylinder.

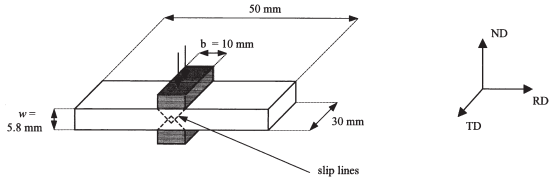

Fig. 3. PSC configuration.

$1\ s^{-1}$, for both SQ and RQ samples. MoS_2 combined with graphite was used as lubricant between the tools and the specimen. Reaching a homogeneous temperature took about 15 min so that samples were deformed only after some annealing. After deformation, the samples were air-cooled and the crystallographic texture was measured systematically at mid-thickness of the specimens. Going from $0.1\ s^{-1}$ to $1\ s^{-1}$ did not significantly change the results in terms of texture evolution or microstructure evolution.

2.2.2. Final textures. Fig. 4 gives the three different types of (0002) pole figure obtained after PSC tests. The first type [Fig. 4(A)] is the most common one and refers to SQ samples. Most of the c-axes are close to the ND. The second and third types [Fig. 4(B) and (C)] refer to RQ samples. In these cases, a texture component appears with c-axes close to the TD (hereafter, we shall call this component a "T" texture component). At 923 K, other maxima appear close to the RD as well [Fig. 4(B)], but they disappear at 1023 K [Fig. 4(C)].

The effect of a 1 h annealing at 1023 K prior to deformation at 923 K was also investigated. Some differences were observed only in RQ samples for which TD- and RD-oriented basal maxima tend to decrease as shown in Fig. 5.

2.2.3. Recrystallization. Samples deformed in the 873–973 K interval retained the lamellar character of the initial Widmanstätten structure. This indicates that no recrystallization took place during or after deformation. Samples deformed at 1023 K, however, showed a non-negligible volume fraction of recrystallization as seen in Fig. 6. This means that, with strain rates of $0.1\ s^{-1}$ and $1\ s^{-1}$, the effects of deformation and recrystallization could only be decoupled at temperatures less than or equal to 973 K.

2.3. Analysis of individual crystallographic orientations in extruded samples, as a function of the microstructure

The PSC tests led most of the time to non-recrystallized microstructures with high dislocation den-

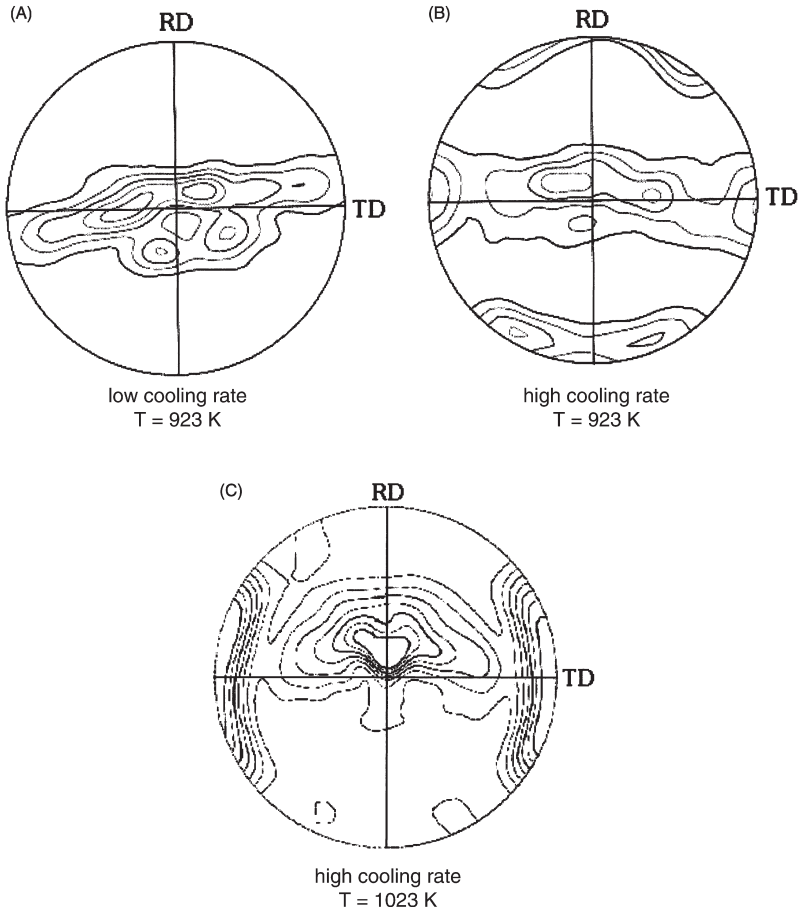

Fig. 4. Typical (0002) pole figures obtained after PSC test. The samples were previously cooled from the β-phase at a low (A) or high rate (B, C) (SQ and RQ microstructures, respectively), and deformed at various temperatures. The rolling, transverse and normal directions (RD, TD and ND respectively) refer to those shown in Fig. 3. Level lines are given in (A) and (B) as multiples of random distribution (mrd), and in (C) as 0.5 mrd.

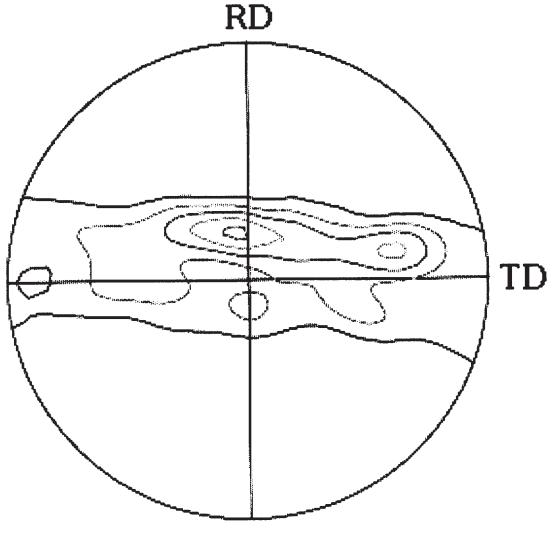

Fig. 5. Effect of prior annealing (1 h at 1023 K) on the PSC texture, for case (B) in Fig. 4.

sities. TEM observations of such materials are therefore not easy, and crystallographic orientations are difficult to identify from TEM or electron backscatter pattern (EBSP) Kikuchi patterns. In contrast, extruded samples have a lower dislocation density because of metadynamic recrystallization and dynamic recovery. The thermally activated processes may of course influence grain crystallographic orientations. In what follows, both the thermally activated processes and the β-quenched microstructural features are investigated in their relationship with grain orientations.

2.3.1. Linking crystallographic orientations to chemical composition using EBSP/EDX techniques.

The surface preparation was different from the one used for optical observations because anodic oxidation must be prevented. After conventional polishing, etching was performed using a solution made of 100 ml H_2O, 23 ml HNO_3 and 2 ml HF applied during approximately 30 s. The grain structure was difficult to reveal by scanning electron microscopy (SEM), and therefore is not presented.

Eighty-three EBSP measurements were performed

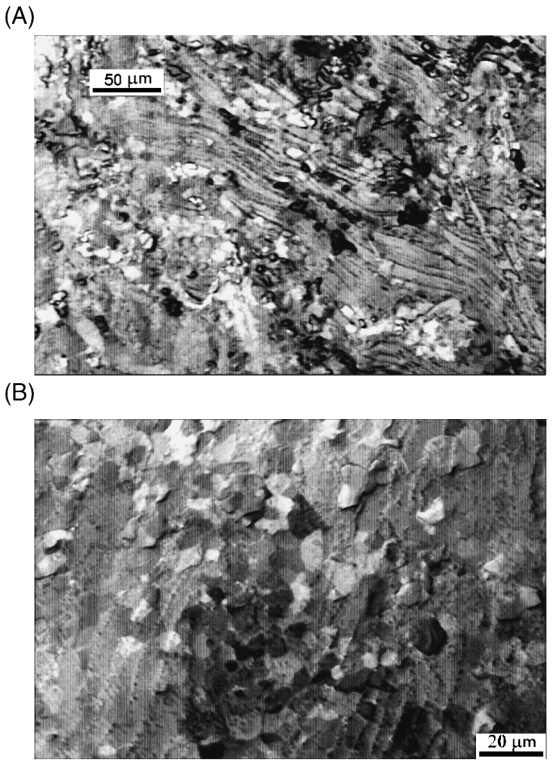

Fig. 6. Partial recrystallization of PSC samples after being deformed at 1023 K.

and are summarized in Fig. 7. The global (0002) and $(10\bar{1}0)$ pole figures are each split into two parts. The splitting procedure depends on the results of a chemical analysis obtained from the electron diffraction X-ray (EDX) technique in the neighborhood of the area where the crystallographic orientation was measured. If a line-scan across the area showed smooth, non-negligible variations of iron and/or chromium content, then the structure was assumed to exhibit, locally, variations of precipitate density. The corresponding area was labeled "FHDP area", in reference to the initial microstructure (see Section 2.1). Fig. 8 illustrates such an FHDP area, with variations of iron content. The measured spot for crystallographic orientation is indicated by a cross in the middle of the line-scan. If, on the contrary, only random, discrete and strong peaks of iron and/or chromium appeared, then the structure was assumed to contain only a few large and isolated precipitates, and the area was labeled "LIP area" (see Section 2.1).

Fig. 7 shows that, with the distinction made from the EDX analyses, the "T" texture component clearly appears to be connected to FHDP areas.

2.3.2. Linking individual crystallographic orientations to dislocation density and precipitate structure, using TEM observations and Kikuchi patterns.

As for EBSP measurements, TEM Kikuchi patterns can be used to identify crystallographic orientations of individual grains with high precision and excellent resolution thanks to the small size of the electron beam [21].

In TEM, the heritage of the Widmanstätten structure is usually very apparent and the former platelets are subdivided into a collection of equiaxed grains because of the combined effect of recovery and recrystallization, as shown in Fig. 9. The long axes of the former platelets are clearly along the axial direction. Some regions have completely recovered or recrystallized and their former platelet envelope has disappeared. It is noticed that some grains exhibit LIP structures while others are closer to an FHDP structure. Of course, FHDP grains are more frequent when the initial microstructure is RQ, as along the external boundary of the tube.

Individual crystallographic orientations were determined from the Kikuchi lines patterns, using the EDTEM code developed by Zaefferer and Schwarzer [21]. Several zones were analyzed, in order to identify possible rules linking the grain microstructural state to the "T" orientation; i.e., the orientation of FHDP areas in Fig. 7.

Fig. 10 gives the result of the analysis for 94 grains over an area of about 300 μm^2 corresponding to only a few platelets of the initial microstructure (see Section 2.1). It is shown here that these 94 grains reasonably account for the global texture, which indicates that a grain refinement has taken place and has led to very distinct orientations. Indeed, the substructure formed within the former platelet structure is made of highly misoriented neighboring grains.

The grain structure refinement observed is the consequence of dislocation structure reorganizations taking place during and after deformation, which may influence the final texture. We therefore measured grain dislocation densities and tried to correlate them to crystallographic orientations. The result was negative. Instead of looking at the dislocation densities, we then examined the distribution of precipitates. FHDP and LIP grains were considered separately and, even if this distinction was not always easy to make, we found that most of the typical FHDP grains had a "T" orientation. These grains are illustrated at three different scales in Fig. 11. Thus we confirmed with this TEM study that the FHDP areas previously measured on the SEM indeed correspond to regions exhibiting fine and homogeneously distributed precipitates.

3. TEXTURE CALCULATION

3.1. The polycrystalline viscoplastic self-consistent model

The self-consistent model developed by Lebensohn and Tomé [18] takes into account the interaction between each grain and the surrounding anisotropic polycrystal. This interaction is based on an Eshelby-type approach, each grain being considered as an elliptic inclusion embedded in a matrix having the average properties of the polycrystal. The two-site

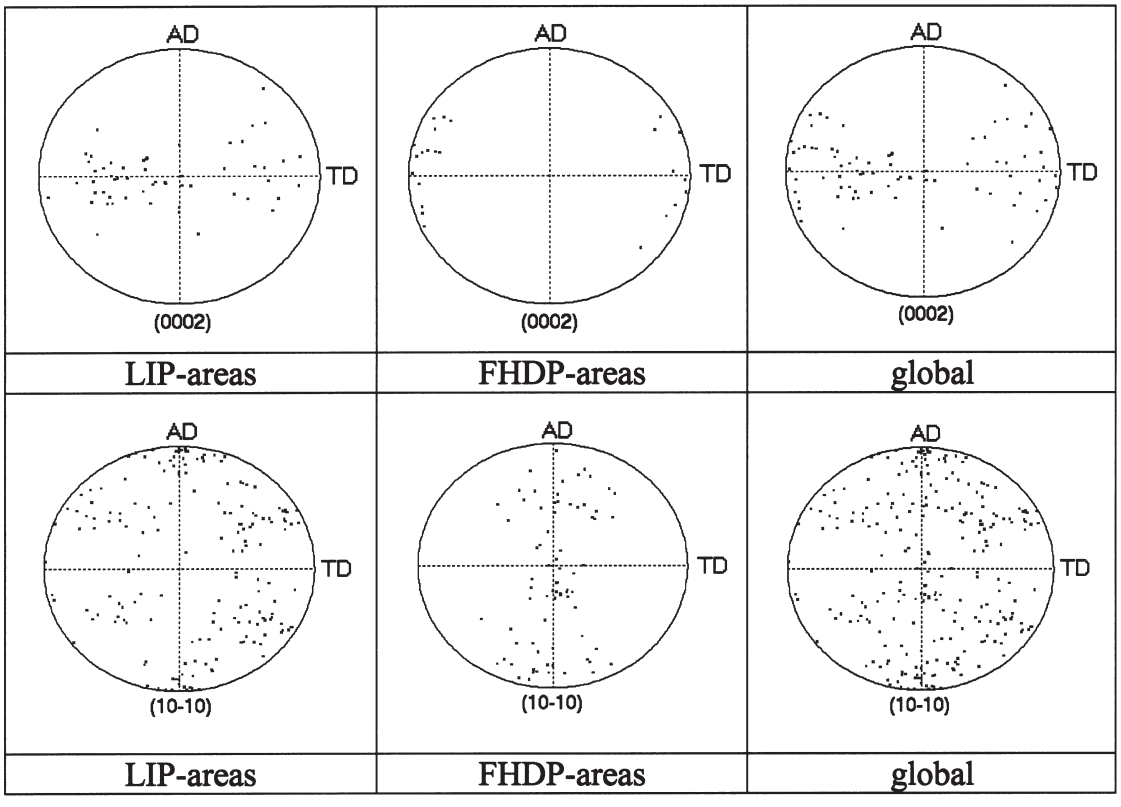

Fig. 7. (0002) and (10$\bar{1}$0) poles from EBSP measurements. Distinction is made between LIP areas and FHDP areas.

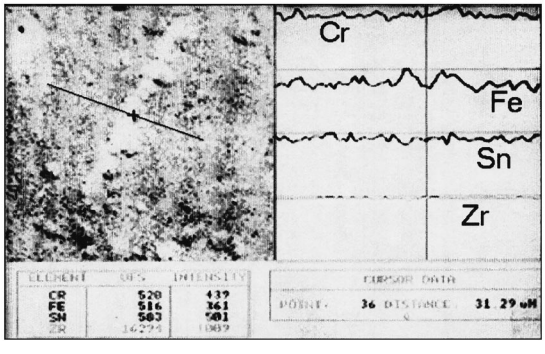

Fig. 8. Typical EDX line-scan showing variations of Sn, Fe and Cr concentrations in an extruded sample, across an FHDP area.

version of the code differs from the one-site approach by the introduction of a second inclusion representing the close neighborhood of the grain [22]. The two adjacent inclusions may have specific orientation relationships. The two-site approach is therefore suitable when two phases spatially close to each other have defined morphological and crystallographic relationships. When this information is not available or when the type of microstructure does not fit within this description, the one-site approach may be used by simply specifying the volume fraction of the different phases and the corresponding crystallographic description of the active deformation modes. In what follows, the calculation is made using the one-site version of the polycrystalline model.

The initial texture of a polycrystal is represented by a set of discrete orientations (or grains) characterized by a set of three Euler angles and a weight associated with the corresponding volume fractions. In this work, a set of 1000 random orientations with equal weights was used for the initial texture, as it is usually observed that the β-quenching operation more or less randomizes the texture (see Fig. 2).

As in [23], the assumed active deformation modes are $\{10\bar{1}0\}\langle 1\bar{2}10\rangle$ prismatic slip, $\{0001\}\langle 1\bar{2}10\rangle$ basal slip, $\{10\bar{1}1\}\langle 1\bar{2}\bar{1}0\rangle$ pyramidal slip in the $\langle a\rangle$ direction, and $\{10\bar{1}1\}\langle 11\bar{2}3\rangle$ pyramidal slip in the $\langle c + a\rangle$ direction. These deformation modes will be referred to as pr$\langle a\rangle$, bas$\langle a\rangle$, pyr$\langle a\rangle$ and pyr$\langle c + a\rangle$, respectively. Pyr-$\langle a\rangle$ slip is usually not considered to be active at temperatures above 873 K because of the increasing activation of basal slip [14]. However, non-negligible cross slip in the pyramidal planes may play a role in accommodating basal shears, especially in the presence of alloying elements in solid solution, as will be discussed later.

3.2. Plane strain compression test

In principle, the velocity gradient matrix describing the PSC test is complex, due to the friction effects. From torsion tests [24], it is known that shearing may

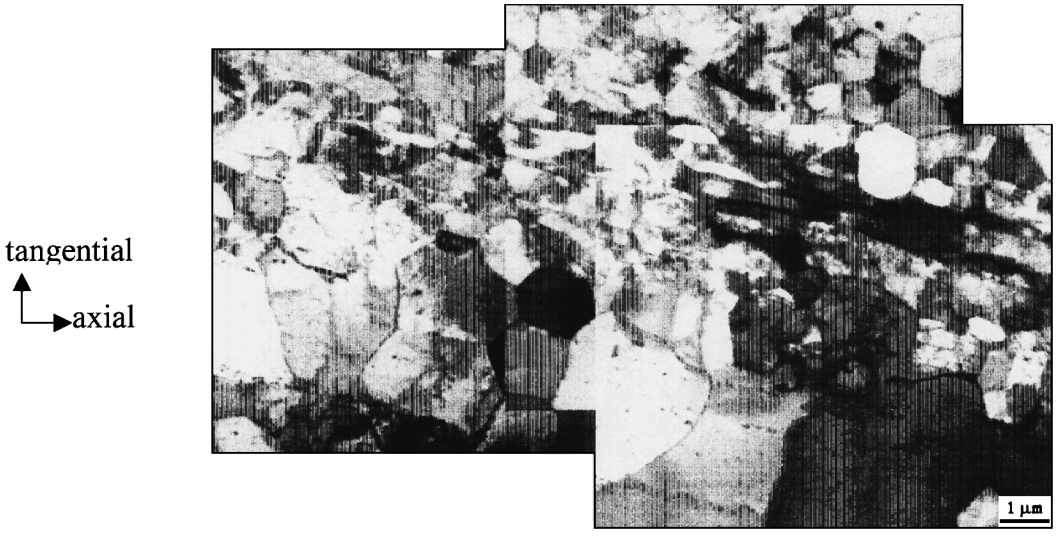

Fig. 9. TEM images showing a typical microstructure after hot extrusion: a mixture of elongated platelets with recovered and recrystallized grains.

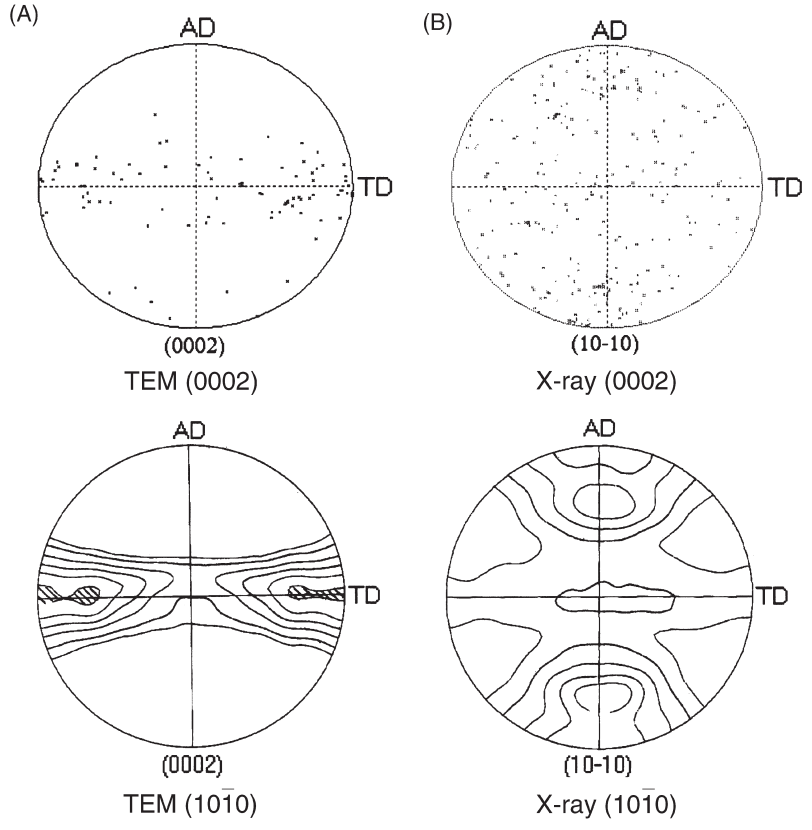

Fig. 10. (0002) and (10$\bar{1}$0) pole figures corresponding to: (A) measured individual grain orientations using TEM and (B) a global X-ray measurement.

lead to a non-orthotropic (0002) pole figure, with the basal poles localized near the ND. However, the simulation was used to reproduce the microstructure effects on texture evolution, reported in Fig. 4. The influence of friction effects was therefore neglected for this purpose.

Simulations [6] have already shown that it is possible to match the (0002) pole figure of Fig. 4(A) with a realistic set of critical resolved shear stresses (CRSS). The other two pole figures in Fig. 4(B) and (C) are not as easy to reproduce. An inverse method developed by Signorelli *et al.* [25] was applied to the

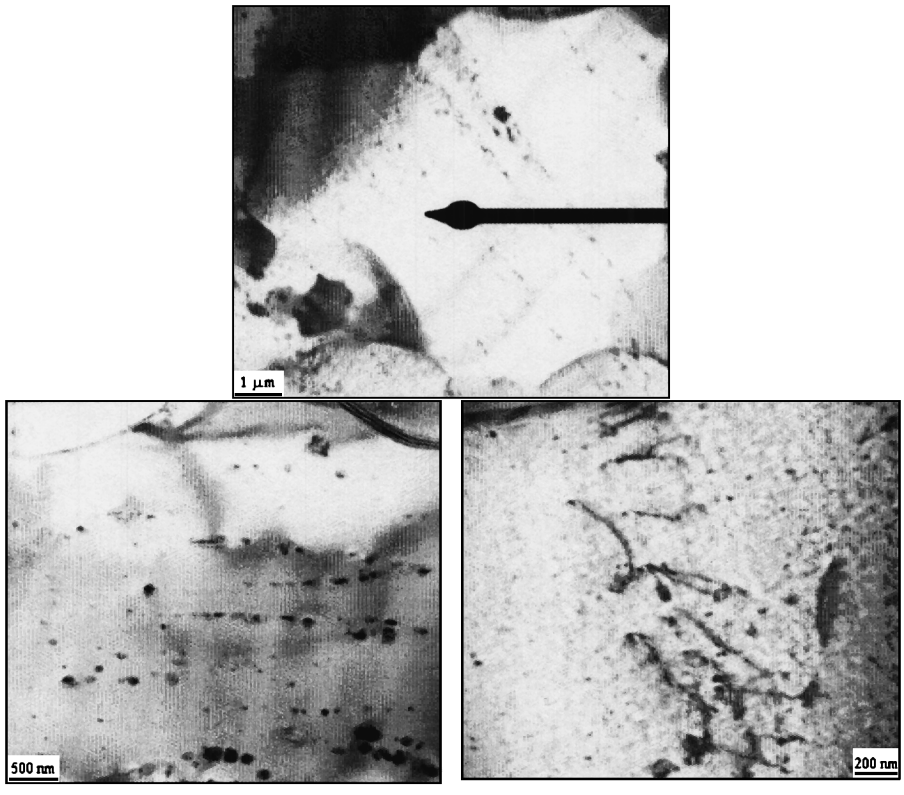

Fig. 11. Examples of FHDP grains exhibiting a "T" orientation. Each image is at a different scale.

latter experimental results to decide if any selection of CRSS may produce the required texture components, assuming the four active slip systems described previously, and a microscopic strain-rate sensitivity of 0.14. The result of the calculation was negative, which might be attributed to some inadequacy of the self-consistent model. However, the microstructure examinations reported in Section 2 have shown that it is meaningful to consider the β-quenched material as made of two different classes of grains, the LIP and FHDP grains. As the deformation proceeds, they systematically form distinct texture components, and must therefore have distinct properties. The β-quenched material is in that respect *heterogeneous*. Consequently, the *two-phase* version of the model was used, taking the CRSS reported previously [6] for LIP regions and a new set of CRSS for FHDP regions. In the latter regions, the effect of iron was thought to favor pyramidal slip, as will be discussed later. Since prismatic slip is always the principal deformation mode in zirconium alloys, pr⟨a⟩, pyr⟨a⟩ and pyr⟨c + a⟩ slip systems were considered to be active in FHDP regions, but the basal slip systems were not. The best fit with experimental results was obtained with the CRSS values reported in Table 2.

The calculated (0002) pole figures are shown in Fig. 12 for various relative volume fractions of the two classes of grain. Increasing the FHDP volume fraction leads to stronger "T" texture components. Tables 3 and 4 show, on the other hand, that the sum of pyr⟨a⟩ and bas⟨a⟩ activities remains more or less constant, regardless of the FHDP volume fraction. In contrast, pyr⟨c + a⟩ activity increases with FHDP volume fraction. The calculation indicates that this activity also increases with strain, and results in an "A"-texture component; i.e., c-axes close to the RD.

3.3. Extrusion textures

Using the set of CRSS presented in Table 2 it is possible to calculate textures at various thickness levels of an extruded tube. Of course, the calculation only takes into account the effect of the precipitates' structure, and not the thermally activated processes.

The deformation path was evaluated quantitatively

Table 2. CRSS values in the LIP/FHDP model

	Pr⟨a⟩	Bas⟨a⟩	Pyr⟨a⟩	Pyr⟨c + a⟩
LIP regions	1	1.5	–	10
FHDP regions	1	–	2	5.5

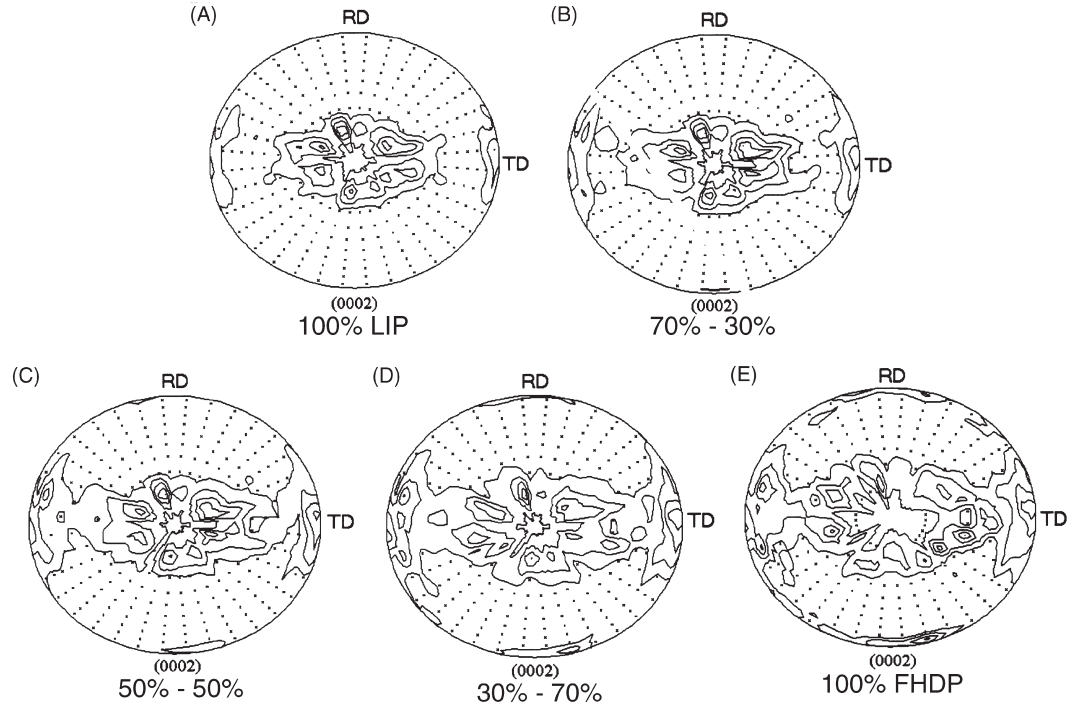

Fig. 12. Calculated PSC (0002) pole figures for various proportions of LIP/FHDP regions. FHDP volume fraction increases from (A) to (E).

Table 3. Calculated average activities of the different deformation modes during the PSC test, with 50% LIP and 50% FHDP

	Pr⟨a⟩	Bas⟨a⟩	Pyr⟨a⟩	Pyr⟨c + a⟩
LIP regions	0.32	0.25	–	10^{-4}
FHDP regions	0.31	–	0.11	0.01

Table 4. Calculated average activities of the different deformation modes during the PSC test, with 100% FHDP

Pr⟨a⟩	Pyr⟨a⟩	Pyr < c + a >
0.61	0.34	0.05

by using a Eulerian finite element formulation such as LAM3 [26] and assuming a steady-state flow. Knowing the friction coefficients between the die and the material, a sequence of velocity gradients was calculated along various streamlines [24]. The texture evolution was then computed along streamlines at the inner and outer surfaces of the tubes and at mid-thickness. The results are presented in Fig. 13 and compared with experimental measurements. Recall that, prior to hole drilling and extrusion, the cylindrical part was water-quenched from the β-phase so that the cooling rates were higher at the surface than in the center of the cylinder. Bearing in mind that the cylinder should then display a microstructure gradient, the relative volume fractions of LIP and FHDP regions were varied along the radius of the tube.

Fig. 13 shows that the calculation can reasonably reproduce the c-axes distribution in the plane perpendicular to the axial direction (AD). However, the "A"-texture component associated with c-axes close to AD is not found experimentally. As explained in Section 3.2 for the PSC tests, this "A" component is generated by the pyr⟨c + a⟩ activity in the FHDP regions at large deformations. The intensity level appears very high because all grains take almost exactly the same orientation. However, even along the outer surface where the FHDP/LIP ratio is maximum, the "A"-texture component does not represent more than 23% of the total volume fraction.

4. DISCUSSION

4.1. Effect of metadynamic recrystallization

Given the results of Section 3.3, it is assumed that the "A"-texture component is removed after extrusion, due to metadynamic recrystallization. This assumption is further supported by several experimental facts, as presented below.

1. The PSC textures in Fig. 4(B) (RQ sample,

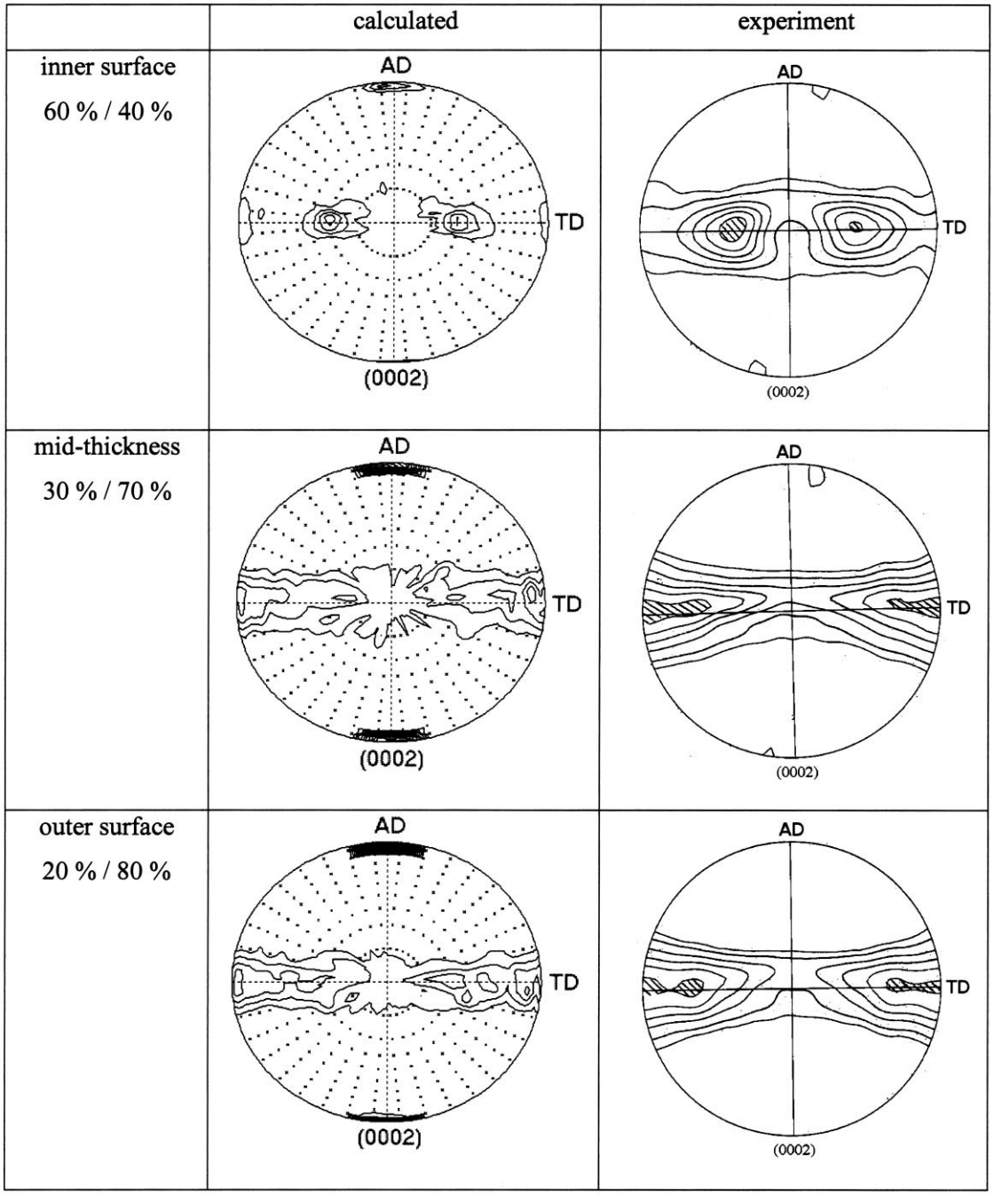

Fig. 13. Calculated and experimental extrusion textures. The volume fractions of LIP/FHDP regions are chosen according to the cooling rate during β-quenching.

deformed at 923 K) and Fig. 4(C) (RQ sample, deformed at 1023 K) show that the "A" orientations have disappeared while recrystallization has appeared, as seen in Fig. 6.

2. Annealing experiments were performed on extruded samples only partially recrystallized (i.e., recrystallized fractions of about 50%). The annealed textures showed a significant weakening of "A"-type texture components while the distribution of c-axes in the radial–tangent (RD–TD) plane remained about the same.
3. An extrusion process was stopped while the material was still flowing inside the extrusion die. The material cooled down because of heat conduction, and the cooling rate was in turn faster than the one induced by air convection. Using TEM it

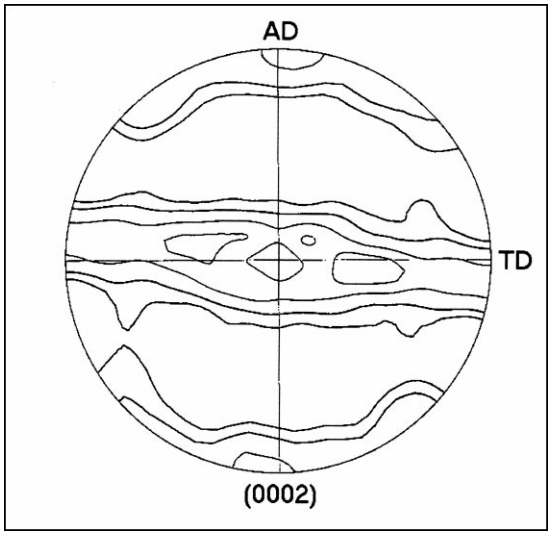

Fig. 14. (0002) pole figure of a partially extruded sample, with no metadynamic recrystallization (internal boundary).

was checked that such a cooling rate prevented recrystallization. The associated texture measurements showed a pronounced "A"-texture component, as seen in Fig. 14.

A tentative explanation of the Zircaloy-4 recrystallization behavior may be given in terms of the theory developed by Lee [27] which, so far, has been used only for cubic materials (e.g., [28]). The model is based on the assumption that the nuclei that grow during recrystallization will have orientations minimizing the elastic energy related to the dislocations' stress field in the surrounding parent grain. This stress field is considered to be of highest intensity in the direction parallel to that of the average Burgers vector. To minimize the energy, a growing nucleus will have its direction of minimum Young's modulus aligned with the direction of maximum stress. In zirconium in the temperature range of interest, the Young's modulus is minimum in the basal plane and maximum along the c-axis [1]. The ratio of maximum to minimum is approximately 2. According to the model, only when a non-negligible pyr$\langle c + a \rangle$ activity has occurred would c-axis reorientation take place during recrystallization. Since we know this is the case for "A"-oriented grains, it is not surprising to see them disappear during recrystallization.

4.2. Precipitation and slip activity

According to the calculation, pyr$\langle c + a \rangle$ slip is only quite active in the FHDP regions (see Tables 2–4). More generally, we may discuss the physical reasons for the differences in CRSS for FHDP and LIP regions on the basis of previous work reported in the literature.

At low temperature, the effect of oxygen on the active deformation modes in titanium has been explained [29]. When interstitial sites are filled by oxygen atoms they reduce both basal and prismatic slip, but do not greatly influence pyramidal slip, as long as the solute concentration remains low. As a consequence, pyramidal slip is favored. The preferential selection of the pyramidal planes due to oxygen content has been observed in the Ti–6Al–4V alloy at low and intermediate temperatures [30, 31]. On the other hand, in cold-rolled zirconium and Zircaloy, cross slip from a prismatic to a pyramidal plane with a common $\langle a \rangle$ Burgers vector was observed [32] using TEM. Further, this cross slip was more active with increasing oxygen content. It was also noted that pyr$\langle c + a \rangle$ glide was frequent when twinning did not occur. These experimental results show that the effect of interstitial oxygen is similar in zirconium and titanium alloys.

Dynamic strain aging has been reported in Zircaloy-4 over the temperature range we are concerned with [33]. It was shown that the extent of this phenomenon was inversely proportional to the amount of iron in the second-phase particles [33]. Also, *a finer dispersion and smaller volume fraction of these particles*—i.e., an FHDP microstructure in our vocabulary—were found to promote strain aging. This effect was correlated with the formation of Cottrell atmospheres around dislocations, created by the iron present in solid solution, and implies that iron diffusion in zirconium is faster than the self-diffusion of zirconium in the high-temperature range. This has subsequently been confirmed experimentally [34]. Moreover, it has been shown that iron atoms start dissolving from Zr_3Fe precipitates in α-Zr in a temperature interval close to 923 K and then enter the solid solution as interstitials [35]. This supports the idea of an interaction between dislocations and iron atoms present in the zirconium matrix as *interstitials*, as is usually the case in strain aging, and not as *substitutional* elements as was assumed by Garde [33].

According to [36], $Zr(Fe,Cr)_2$ precipitates in Zy4 quenched from the β-phase have a face-centered cubic (fcc) structure C15 which evolves with subsequent annealing towards the hcp structure C14. As this transformation proceeds, more iron atoms diffuse into $Zr(Fe,Cr)_2$ precipitates and a second type of iron-bearing particle appears at the same time. Annealing prior to deformation is therefore able to modify the structure, composition and size of Fe-based precipitates. The variation in size is related to a change of spatial distribution of these precipitates [37, 38], and therefore to a change of LIP/FHDP volume fractions [see Fig. 5, compare with Fig. 4(B)]. This is analogous to the segregation phenomena of iron-rich precipitates that have been observed by Hood and Schultz [39] in Zr–0.1 at% Fe single crystals, supersaturated in Fe. Pre-annealing at 1100 K yielded an inhomogeneous distribution of the precipitates throughout the bulk of the material. Single-crystal specimens were then extracted, ground, polished and subjected to additional annealing. This induced a *re-*

precipitation process of iron from the bulk to the surface of the crystals. The pre-annealing effect on iron distribution was attributed to a material "partly transparent and partly opaque" to the emission of iron to the surface. Other experiments using thermoelectric power measurements [16] detected precipitation phenomena at the platelet boundaries of β-quenched samples. Around 923 K, the phenomenon took only a few minutes. However, the amount precipitated corresponded to only about 150 ppm of solute, and was related to precipitation of the excess iron and/or chromium atoms in solid solution that remained after quenching. As seen in Fig. 1, precipitation at the platelet boundaries does not mean that there is no FHDP structure.

The above studies lead us to the interpretation that FHDP regions are those where the mean diffusion length of iron atoms, released from the precipitates, is comparable to the average precipitate spacing. Most of the volume fraction of the material is then influenced by diffusing iron atoms. Since they can interact with moving dislocations, they can also modify the relative CRSS, as oxygen does at lower temperature. Their assumed effect is to make pyramidal slip easier, as explained elsewhere [29], and to inhibit basal slip. The latter effect may be related to the lower diffusion coefficient of iron in the direction perpendicular to the c-axis, compared with the value in the direction parallel to the c-axis [34]. If one looks at basal slip as the result of cross slip from a prismatic plane [14], the basal plane should be sensitive to any dislocation obstacle and easily inhibited when other slip planes are available.

4.3. The extended polycrystalline model

The LIP/FHDP model presented in Section 3 had the primary purpose to support the SEM and TEM studies of Section 2.3 made on extruded samples. It showed that, even when no recrystallization takes place as in the PSC tests, the distinction between LIP and FHDP regions is useful and allows one to explain the observed microstructure dependency of texture evolution. In other words, the conclusion that LIP and FHDP grains evolve towards different texture components was not influenced by the effects of thermally activated processes. This, in turn, gave the possibility of using the model to predict extrusion textures and to deduce recrystallization effects.

In doing so, we have introduced a simple model which accounts for the precipitate structure, with the FHDP volume fraction depending on the cooling rate from the β-phase. Also, the CRSS values used in the model can be justified on the basis of previous work reported in Section 4.2. In what follows, we therefore examine some details of the texture calculations found in Section 3, and discuss further the LIP/FHDP model.

According to our calculations, and as is generally agreed for zirconium alloys [6], prismatic slip is the predominant slip mode. Basal slip is on average the second most active slip system, but is restricted to LIP regions or to regions without precipitates, while pyramidal slip activity becomes significant only in FHDP regions. The important feature enforced in the polycrystalline model was to remove basal slip for the FHDP regions. Should the prismatic slip be very active, *a grain-shape effect* can then promote rotation of the c-axes towards the TD [22]. On the contrary, when basal slip is significant, reorientation always tends to push c-axes close to the major compression axis. It is interesting to notice that basal slip is traditionally believed to be more and more active as the temperature approaches the $\alpha \rightarrow \beta$ phase transition [14]. We find here that, for the particular FHDP regions in Widmanstätten microstructures, increasing temperature leads to an increase in both the amount of iron dissolved from precipitates and the diffusion length of iron. This then leads to an overall *decrease* in basal activity, which is consistent with observed variations of extrusion textures with extrusion temperature [11]. When the phase transition has occurred, a similar argument can be invoked to understand the formation of "T" textures. Indeed, it has been shown that the presence of a softer β-phase leads to an increase in prismatic activity in the α-phase of lamellar titanium alloys [22].

A grain subdivision mechanism has been described in Section 2.3.2, where the platelet structure splits up with deformation into "cells" of increasing misorientation, thereby transforming those cells into real grains. Such a phenomenon has been observed in other materials (e.g., [40, 41]) and is designated as "extended recovery" or "continuous recrystallization". Unlike *discontinuous* recrystallization, this phenomenon does not prevent the formation of pronounced textures and its effects on the texture evolution have therefore not been explicitly considered. However, the resulting highly misoriented substructure allows us to approximate the properties in the immediate neighborhood of the grains by the polycrystal properties (see Fig. 10), and to validate the so-called one-site approximation in the self-consistent model [18].

Finally, one should note that the proposed LIP/FHDP model for Widmanstätten structures has introduced an additional degree of freedom, namely the volume fraction of FHDP regions. It may be argued that this volume fraction represents a fitting parameter, since no independent validation of the model was presented. However, as stated above, the FHDP volume fraction may be evaluated as a direct function of the cooling rate during β-quenching and of subsequent annealing time. We believe that a single value can be used for a given microstructure to simulate various deformation modes, including the more complex ones such as extrusion. For example, the FDHP volume fractions reported in Fig. 13 have shown a good agreement with those assessed from torsion tests, where we took advantage of the axial effects resulting from the texture-induced anisotropy.

The latter procedure will be discussed in a future paper.

5. CONCLUSIONS

In this study we have shown that microstructure considerations may become very important for the control of texture evolution in high-temperature forming processes involving zirconium-based alloys. The role of β-quenching prior to deformation is emphasized, both in terms of microscopic deformation modes and texture evolution. An LIP/FHDP model is presented and calculated texture evolution agrees with experimental measurements for plane strain compression laboratory tests. The same model is used to predict hot extrusion textures at different thickness levels of the tubes, and suggests an effect of metadynamic recrystallization on the deformation-induced texture.

A detailed explanation of the influence of the precipitate structure on high-temperature texture evolution of zirconium-based alloys is still needed. A few clues have been proposed, based on existing work, and are consistent with the LIP/FHDP model. It is clear, however, that the phenomenological approach adopted here, essentially based on the variation of CRSS values, should be confirmed and/or improved by additional appropriate microscopic observations associated with intra-crystalline modeling.

Acknowledgements—The authors wish to thank Cezus Company for their global support of this work. They are especially grateful to Denis Gex, from Ugine Savoie, for the texture measurements. Dr S. Zaefferer is also acknowledged for providing his EDTEM code, together with Dr T. Cutard and Dr P. Lamesle for their contribution in the EBSP measurements. Special thanks also go to Professor P. R. Dawson for his very useful comments on the manuscript. The study received funding from the European Commission through a TMR Marie Curie research training grant (R. Logé), and from the ECOS–SCYT co-operation program between France and Argentina (J. Signorelli, Y. Chastel, R. Lebensohn).

REFERENCES

1. Turner, P. A., Christodoulou, N. and Tomé, C. N., *Int. J. Plast.*, 1995, **11**, 251–265.
2. Akhtar, A., *J. Nucl. Mater.*, 1973, **47**, 79.
3. Tenckhoff, E., in *Zirconium in the Nuclear Industry: 5th Conference*, ed. D. G. Franklin, 1982, p. 5.
4. Cheadle, B. A. and Ells, C. E., *J. Nucl. Mater.*, 1967, **24**, 240.
5. Cheadle, B. A., Aldridge, S. A. and Ells, C. E., *J. Nucl. Mater.*, 1970, **34**, 119.
6. Lebensohn, R. A., Sanchez, P. V. and Pochettino, A. A., *Scripta metall. mater.*, 1994, **30**, 481.
7. Hindle, E. D. and Slattery, G. F., *J. Inst. Met.*, 1965, **93**, 565.
8. Tenckhoff, E. and Rittenhouse, P. L., in *Applications-Related Phenomena for Zirconium and its Alloys*. American Society for Testing and Materials, 1969, p. 50.
9. Cheadle, B. A., Aldridge, S. A. and Ells, C. E., *Can. Metall. Quart.*, 1972, **11**, 121.
10. Holt, R. A. and Aldridge, S. A., *J. Nucl. Mater.*, 1985, **135**, 246.
11. Cezus Company, Internal Report, 1998.
12. Xiao, L. and Gu, H., *Met. Mater. Trans. A*, 1997, **28A**, 1021.
13. Chakravartty, J. K., Banerjee, S., Prasad, Y. V. R. K. and Asundi, M. K., *J. Nucl. Mater.*, 1992, **187**, 260.
14. Akhtar, A., *Acta metall.*, 1973, **21**, 1.
15. Doherty, R. D., Hughes, D. A., Humphreys, F. J., Jonas, J. J., Juul Jensen, D., Kassner, M. E., King, W. E., McNelley, T. R., McQueen, H. J. and Rollett, A. D., *Mater. Sci. Eng.*, 1997, **A238**, 219.
16. Loucif, K., Borrelly, R. and Merle, P., *J. Nucl. Mater.*, 1994, **210**, 84.
17. Ciurchea, D., Pop, A. V., Gheorghiu, C., Furtuna, I., Todica, M., Dinu, A. and Roth, M., *J. Nucl. Mater.*, 1996, **231**, 83.
18. Lebensohn, R. A. and Tomé, C. N., *Acta metall. mater.*, 1993, **41**, 2611.
19. Akhtar, A., *Met. Trans. A*, 1976, **7A**, 1735.
20. Watts, A. B. and Ford, H., *Proc. Inst. Mech. Engrs*, 1955, **169**, 1141.
21. Zaefferer, S. and Schwarzer, R. A., *Mater. Sci. Forum*, 1994, **157-162**, 241.
22. Lebensohn, R. A. and Canova, G. R., *Acta mater.*, 1997, **45**, 3687.
23. Tomé, C. N., Lebensohn, R. A. and Kocks, U. F., *Acta metall. mater.*, 1991, **39**, 2667.
24. Logé, R. E., Ph.D. Thesis. Ecole Nationale Supérieure des Mines de Paris, 1999.
25. Signorelli, J. W., Loge, R. E., Chastel, Y. B. and Lebensohn, R. A., *Model. Simul. Mater. Sci. Eng.*, 2000, **8**, 193.
26. Hacquin, A., Ph.D. Thesis. Ecole Nationale Supérieure des Mines de Paris, 1996.
27. Lee, D. N., *Scripta metall. mater.*, 1995, **32**, 1689.
28. Choi, C. -H. and Lee, D. N., *Met. Mater. Trans. A*, 1997, **28A**, 2217.
29. Churchman, A. T., *Proc. R. Soc.*, 1954, **A226**, 216.
30. Welsch, G. and Bunk, W., *Metall. Trans. A*, 1982, **13A**, 889.
31. Lecomte, J. S., Philippe, M. J. and Klimanek, P., *Mater. Sci. Eng.*, 1997, **A234-236**, 869.
32. Philippe, M. J., Esling, C. and Hocheid, B., *Text. Microstr.*, 1988, **7**, 265.
33. Garde, A. M., *J. Nucl. Mater.*, 1979, **80**, 195.
34. Hood, G. M. and Schultz, R. J., in *Zirconium in the Nuclear Industry: 8th International Symposium*, eds L. F. P. Van Swam and C. M. Eucken, 1989, p. 435.
35. Vogl, G., Sugimoto, M. and Yoshida, Y., *J. Nucl. Mater.*, 1993, **199**, 112.
36. Xiao, W. and Ma, C., *J. Nucl. Mater.*, 1998, **255**, 67.
37. Wang, C. T., Eucken, C. M. and Graham, R. A., in *Zirconium in the Nuclear Industry: 9th International Symposium*, eds C. M. Eucken and A. M. Garde, 1991, p. 319.
38. Huang, P. Y., Mahmood, S. T. and Adamson, R. B., in *Zirconium in the Nuclear Industry: 11th International Symposium*, eds E. R. Bradley and G. P. Sabol, 1996, p. 726.
39. Hood, G. M. and Schultz, R. J., *Defect Diffusion Forum*, 1989, **66-69**, 371.
40. Gourdet, S., Girinon, A. and Montheillet, F., in *Thermec'97, Wollongong, NSW, Australia*, eds T. Chandra and T. Sakai. Minerals, Metals and Materials Society/AIME, Warrendale, PA, USA, 1997, p. 2117.
41. Montheillet, F. and Gourdet, S., *Materials Science and Engineering A*, 2000, **283**(1–2), 274.